

## ARTICLE

## OPEN



# Strengthening cold wakes lead to decreasing trend of tropical cyclone rainfall rates relative to background environmental rainfall rates

Zanhong Ma<sup>1</sup>, Yanluan Lin<sup>2</sup>✉, Jianfang Fei<sup>1</sup>, Yunxia Zheng<sup>3</sup>, Wenchao Chu<sup>2</sup> and Hexin Ye<sup>1</sup>

Tropical cyclone (TC) rainfall is an important component of global precipitation. Based on a 22-year satellite-based record of observed precipitation from 1998 to 2019, we find that composite rainfall rates averaged within 500 km of TCs have increased. However, the background precipitation rate in the TC-affected regions has also increased. Therefore we find, by subtracting the background increase in precipitation rate from the TC precipitation composite, that TC precipitation rates--relative to the background--have decreased, and that TC-related extreme precipitation rates near the TC center have also decreased. Besides TC intensity and environmental sea surface temperature, the TC-induced sea surface cooling, typically formed like a cold wake feature, is indicated to be a potentially important contributor to TC rainfall changes. The cold wake diminishes the upward transport of surface enthalpy flux and leads to a decrease of moisture in the boundary layer, being unfavorable for the rainfall. The relative decreasing rainfall trend of TCs to the background is therefore attributed to the strengthening sea surface cooling induced by TCs. The TC-ocean interaction is suggested to be fully resolved in state-of-the-art global and regional climate models in order to improve TC rainfall simulations and projections.

*npj Climate and Atmospheric Science* (2023)6:131 ; <https://doi.org/10.1038/s41612-023-00460-w>

## INTRODUCTION

The rainfall of tropical cyclones (TCs) is an important component of global precipitation<sup>1,2</sup>. Resultant freshwater flooding is among the most severe threats to human lives and socioeconomic losses<sup>3–5</sup>. This highlights the necessity of improving the current understanding and prediction skills of TC rainfall. Nonetheless, there are still large uncertainties in the characteristics of TC rain rate, which are modulated simultaneously not only by internal factors such as intensity, translation speed, and asymmetry of TCs<sup>6–9</sup>, but also by environmental parameters such as sea surface temperature (SST), humidity and atmospheric stability, etc.<sup>8,10–13</sup>.

There is a robust increasing trend of global precipitation under warmer climates<sup>14,15</sup>. As inferred from the Clausius-Clapeyron relation, the atmosphere can hold more water vapor at higher temperatures, corresponding to a rate of ~7% per degree Celsius. As such, most global and regional climate models have projected increased TC rain rates with global warming<sup>16–20</sup>, wherein Knutson et al.<sup>17</sup> noted that the rain rate within 100 km of the storm center may increase on the order of 20% by 2100. The availability of global satellite observations can provide clues for the robustness of model predictions. In combination with the Tropical Rainfall Measuring Mission (TRMM) product and global atmospheric model simulations, Lin et al.<sup>13</sup> found that although TC rain rate increases with increasing absolute SST, the rainfall area is dominantly controlled by relative SST. Based on a 19-year time series of observational data, Guzman and Jiang<sup>21</sup> suggested a remarkably increasing trend of TC rain rate by ~1.3% per year, which is nonetheless attributed to a combined effect of decreasing inner-core rainfall and increasing rain rate in the rainband region. The decreasing trend of inner-core rain rate of TCs is highlighted in Tu et al.<sup>22</sup>, which indicated that the TC rain rate decreases by ~1.2% per year within ~100–125 km from the

storm center. Consequently, the overall increasing trend of TC system is about 0.4% per year, being much lower than that reported by Guzman and Jiang<sup>21</sup>. Whatever the quantitative discrepancies in previous work, the observed decreasing trend of TC rainfall in the inner core contradicts the steadily increasing TC rainfall by model projections. There could be important physical processes that occur in the real world but are not resolved in climate models, as also cautioned by Knutson et al.<sup>17</sup>.

TCs are strongly rotating systems with intense inertial stability in the inner core that protects the TCs from possible environmental influences<sup>23,24</sup>. Since the decreasing trend of TC rain rate is most significant near the storm center, diminishing radially outward monotonically (Fig. 1a, b), the dominant contributor should be capable of affecting TC inner core directly, such as the sea surface cooling (SSC) underlying a translating TC. Under global warming, the sea surface warms at a greater rate than the subsurface water, causing a strengthening of upper-ocean stratification<sup>25</sup>. This contributes to a significant increase in global TC-induced SSC<sup>26</sup>. The enhanced cold wakes by TCs have offset a small part of TC intensity increase under global warming conditions<sup>27,28</sup>, while their effect on TC precipitation remains unclear. The contribution of SSC to TC rainfall will be examined in this study, with a comparison to the background rainfall. For each TC location, a square domain with widths of 20° centered around the TC center is used to derive TC rainfall; the background rainfall is derived using the same domain, but with the precipitation data shifted from one year before. Therefore, the background rainfall covers a time period one year shorter than TC rainfall (see section 4 for more details). We will demonstrate in this study that there is a net decreasing rainfall trend of TCs relative to their background environment and that it is the strengthened SSC that leads to the relative decrease of TC rain rate.

<sup>1</sup>College of Meteorology and Oceanography, National University of Defense Technology, Changsha 410073, China. <sup>2</sup>Department of Earth System Science, Tsinghua University, Beijing 100084, China. <sup>3</sup>Shanghai Typhoon Institute, China Meteorological Administration, Shanghai 200030, China. ✉email: yanluan@tsinghua.edu.cn

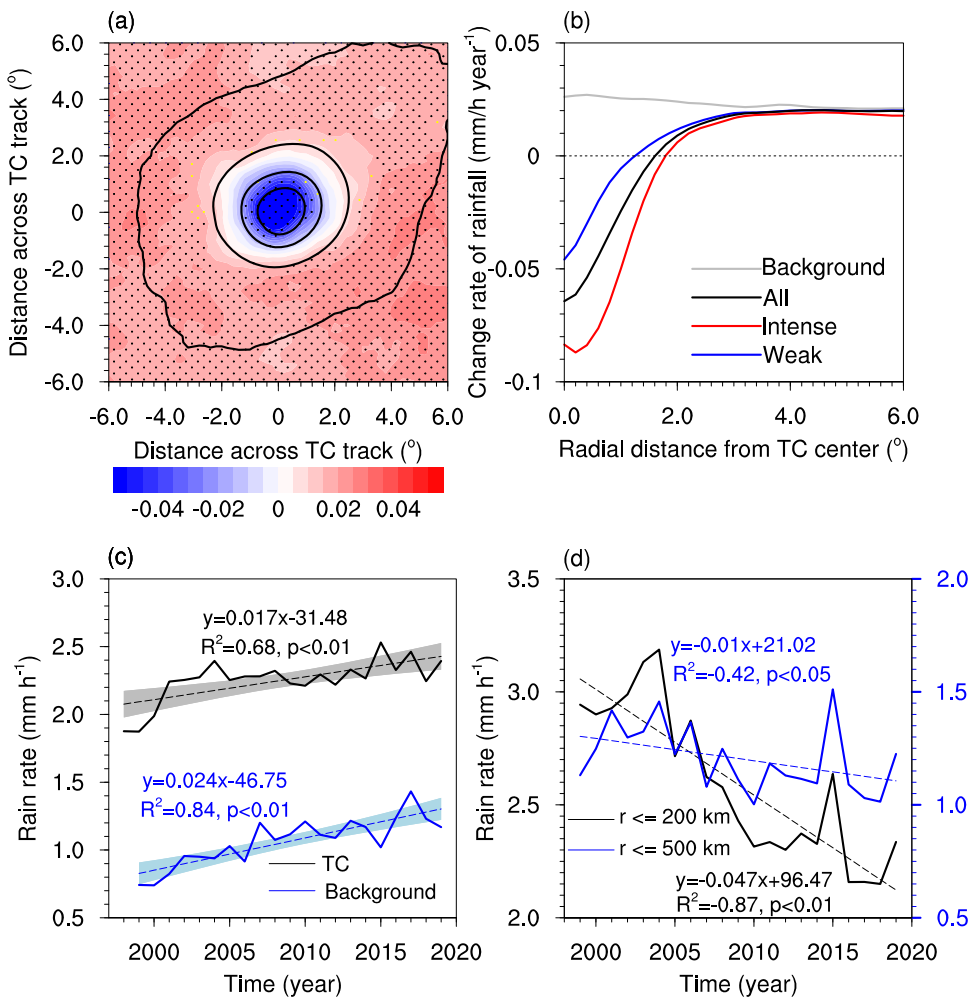


**Fig. 1 Relative decreasing trend of TC rain rate.** **a** Spatial distribution of composite change rate of TC rainfall ( $\text{mm h}^{-1} \text{year}^{-1}$ ; shaded) and TC rain rate ( $\text{mm h}^{-1}$ ; contour) at an interval of  $1 \text{ mm h}^{-1}$ , with the outmost contour being  $1 \text{ mm h}^{-1}$ . Stippling denotes an area where linear trends are statistically significant, with black and yellow dots representing 99% and 95% confidence levels, respectively. **b** Radial distributions of azimuthally averaged change rates of rainfall ( $\text{mm h}^{-1} \text{year}^{-1}$ ) for the background, all TCs, intense TCs (cat 1-5), and weak TCs (cat 0). **c** Time series and linear regression fit of area-averaged TC (black) and background (blue) rain rate ( $\text{mm h}^{-1}$ ). The area averaging is taken within a radius of  $500 \text{ km}$  from TC center for rainy grids. The shading area indicates the two-sided 95% confidence bounds of the trends. **d** Time series and linear regression fit of relative rain rate ( $\text{mm h}^{-1}$ ) for rainy grids averaged within radii of  $200 \text{ km}$  (black) and  $500 \text{ km}$  (blue). The relative rain rate is obtained as the rain rate difference between TCs and the background. The linear fitting function and correlation coefficient in (c) and (d) are also shown. The rainfall data are based on the TRMM product.

## RESULTS

### Relative change rate of TC rainfall to background rainfall

Two precipitation products are used to investigate the change rate of rainfall, one from 22 years of TRMM 3B42 dataset and the other from 20 years of the Global Precipitation Measurement (GPM) dataset (see Methods). The composite rain rates generally increase with TC intensity and increase radially inward to the inner core of TCs (Supplementary Fig. 1). Although the rain rate outside the TC increases positively with time, the change rate of rainfall decreases inward monotonically, turning to be negative within  $1\text{--}2^\circ$  from storm center (Fig. 1a, b). This indicates a decrease of rain rate in the inner core of TCs, consistent with Guzman and Jiang<sup>21</sup> and Tu et al.<sup>22</sup>. The negative change rate of TC rainfall is about  $-0.06 \text{ mm h}^{-1}$  per year near the storm center, corresponding to a remarkable decrease of  $\sim 1.5\%$  per year. Both the positive trends outside TCs and negative trends in the inner core of TCs are mostly statistically significant, except for the transition region in which the change rate declines inward smoothly. This cannot be attributed to the expansion of eye and eyewall, since there would be a notable increase outside the negative region in that case.

A comparison between TCs and the background reveals that the rainfall change rate of TCs is overwhelmingly smaller than that of the background environment, with their difference enlarging radially inward toward the storm center (Fig. 1b and Supplementary Fig. 2). The decreasing trends of TC rainfall relative to the background are apparent in all ocean basins (Supplementary Fig. 3), and there are apparent discrepancies among different basins. The increasing rate of background rainfall is largest over the North Atlantic, while the Southern Hemisphere and Eastern Pacific exhibit the largest decreasing rainfall rates near TC center. The data samples are further classified into weak TCs (CAT 0) and intense TCs (CAT 1-5) based on the Saffir-Simpson scale since the category 0 has accounted for over 60% of all data samples (Supplementary Fig. 4). The decreasing rate of TC rainfall is larger for stronger TCs (Fig. 1b), implying that the physical mechanism leading to the decreasing trend of TC rainfall is related to the intensity characteristics of TCs.

A radius of  $500 \text{ km}$  is conventionally used to define the TC rainfall area<sup>21,29,30</sup>. An average of all rainy grids within this radius shows an evident increasing trend of TC rainfall (Fig. 1c), which is

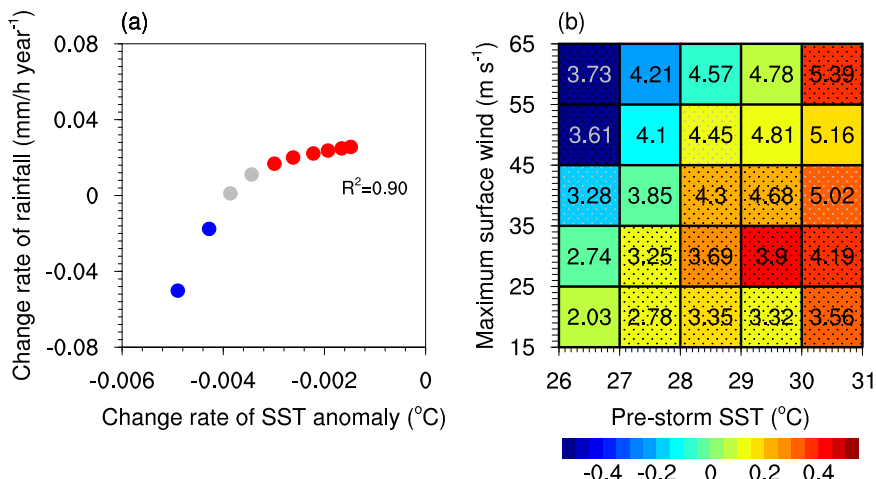


**Fig. 2 Dependence of rain rate on TC intensity and SST anomaly.** **a** Scatterplot of the linear trends of SST anomalies and TC rainfall averaged within radii of 100 km, 200 km, 300 km, 400 km, ..., and 1000 km from the storm center, from left to right. Blue and red dots denote negative and positive trends of TC rainfall, respectively, which are significantly above the 99% confidence level. Gray dots denote the rainfall trends that fail to pass the significant test. **b** Bin plot of linear regression coefficients ( $\text{mm h}^{-1} \text{°C}^{-1}$ ) between TC rain rate and SST anomaly (shaded) averaged within a radius of 200 km from TC center, as functions of pre-storm SST and maximum surface wind. The numerical value in each bin denotes the averaged TC rain rate ( $\text{mm h}^{-1}$ ) by the sub-data sample. The vertical and horizontal grid lines denote bins of data samples classified by pre-storm SST and maximum surface wind at intervals of  $1 \text{ °C}$  and  $10 \text{ m s}^{-1}$ , respectively. Stippling denotes the bin where the correlation is statistically significant, with black and gray dots representing 99% and 95% confidence levels, respectively. The rainfall data are based on the TRMM product.

statistically significant at 99% level. As a result, although the rainfall near the storm center is decreasing, the rain rate for the whole TC system is increasing (Fig. 1a–c and Supplementary Fig. 5). The increasing rate is  $0.017 \text{ mm h}^{-1}$  per year with a coefficient of 0.68, corresponding to an increase by  $\sim 0.76\%$  each year. Of interest is that the background rainfall increases at a greater rate of  $0.024 \text{ mm h}^{-1}$  per year with a larger coefficient of 0.84. As indicated from the radial distributions of rainfall change rate (Fig. 1b), the departure from the environmental trend is increased in the inner core where inertial stability is large, while it approaches zero outside the TC region. This indicates that the increasing trend of TC rainfall is largely attributed to a favorable large-scale environment. Consequently, the relative change rate of TC rainfall after subtracting the background trend is negative, namely a net decreasing trend (Fig. 1d). The decreasing rate of TC rainfall is  $-0.010 \text{ mm h}^{-1}$  per year within a radius of 500 km, but increases to  $-0.047 \text{ mm h}^{-1}$  per year within a radius of 200 km.

The GPM IMERG product is also used to examine the rainfall trend of TCs and the background. Though the GPM possessing larger rain rates than the TRMM product (Supplementary Figs. 1 and 6), there is no apparent positive trend of rainfall either for TCs or for the background environment. For the TRMM product, the rainfall trend is slightly positive outside the TC region or for the background environment (Fig. 1b). The differing rainfall trends between TRMM and GPM (Fig. 1b and Supplementary Fig. 7) also exist in Tu et al.<sup>22</sup> (Fig. 1b), which may be caused by different satellite sources or processing procedures. The change rate of TC rainfall in GPM is more significant for more intense TCs, similar to that of TRMM product. The decreasing rate of TC rainfall diminishes radially outward to be comparable to that of the background rainfall (Supplementary Fig. 7). This at least indicates that the rainfall change rate in the outer region of TCs largely complies with the background and that there is a relative decreasing trend of TC rainfall compared with the background.

### Dependence of TC rain rate on SST anomaly

As discussed above, TC rainfall is influenced by various factors, among which the TC intensity could be the most salient one. In the recent two decades, TC intensity and translation speed

Z. Ma et al.

averaged over all data samples do not show a detectable trend (Supplementary Fig. 8), and there is no evident change in the proportion of different intensity categories (Supplementary Fig. 4). The decrease of TC inner-core rainfall was proposed to be attributed to atmospheric stability<sup>22</sup>, which, however, is recently argued to merely play a minor role<sup>31</sup>. Note that the rainfall change rate of TCs is smaller than that of the background environment not only in the inner core but also in the outer region. The undetectable trend of TC intensity with increasing absolute SST, and the significant decrease of TC rainfall toward the storm center, give a hint that the mechanism leading to the relative decreasing trend of TC rainfall is not only detrimental to TC intensification but also most pronounced near the storm center. The variation of SST could be an ideal candidate contributor<sup>13</sup>. A further examination reveals that there is a strong linkage between the change rate of TC rainfall and that of TC-induced SST anomaly, with their correlation coefficient reaching 0.9 (Fig. 2a). Since the supply of surface enthalpy flux depends on both surface wind speed and air-sea enthalpy disequilibrium<sup>32,33</sup>, TC rainfall decreases remarkably with increasing SSC. This indicates a greater sensitivity of TC rainfall to SST perturbation in the inner TC region.

Since the departure of rainfall trend between TCs and the background is more pronounced in the inner core (Fig. 1b), the TC-related rainfall, pre-storm SST, and TC-induced SST anomaly are averaged with a radius of 200 km to examine their possible relations. The averaged TC rainfall is shown to increase steadily with increasing TC intensity and pre-storm SST, in a range of  $\sim 2\text{--}5.4 \text{ mm h}^{-1}$  (Fig. 2b). An interesting feature is that the TC rain rate becomes larger when the pre-storm SST is higher, even if the TC intensity is unchanged. This is partly because a warmer ocean surface could provide more surface moisture flux, and therefore a moister atmosphere. The environmental SST could serve as an indicator of atmosphere moisture, and therefore larger pre-storm SST favors stronger TC rainfall. To exclude the rainfall dependence on TC intensity and environmental SST, all the data samples are classified by TC maximum surface wind and pre-storm SST at bins of  $10 \text{ m s}^{-1}$  and  $1 \text{ °C}$ , respectively. The linear regression coefficients between TC rainfall and TC-induced SST anomaly as well as their correlation coefficients are then calculated in each bin. There are mostly positive linear regression coefficients over the domain,

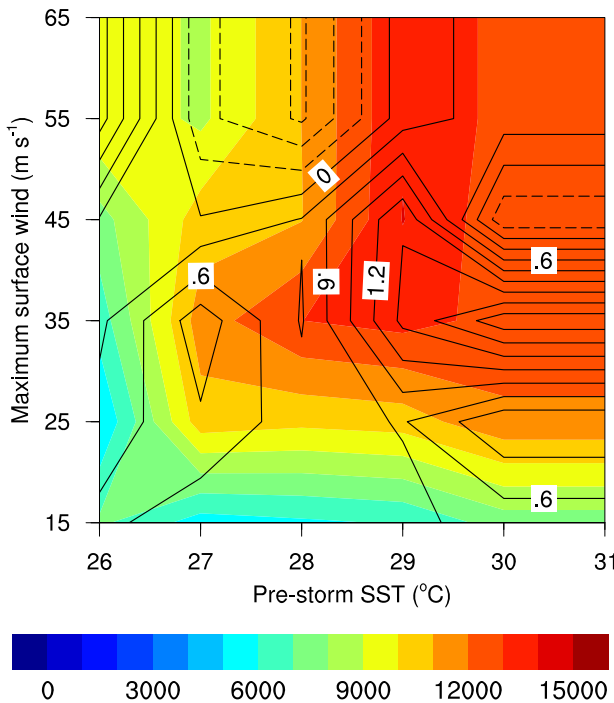


**Fig. 3 Difference of surface enthalpy deficit and boundary layer moisture induced by SST anomaly.** Difference of surface enthalpy deficit (shaded;  $\text{J kg}^{-1}$ ) and boundary layer moisture ( $\text{g kg}^{-1}$ ) as functions of pre-storm SST and maximum surface wind. The difference of surface enthalpy deficit and boundary layer moisture is calculated as the averaged values for the smallest (0–5%) magnitudes of SST anomaly data samples minus that for the largest (95%–100%) SST anomaly data samples in each bin. An area averaging within a radius of 200 km from TC center is taken for each data sample. The definition of surface enthalpy deficit is given in Eq. (2) and discussed in section 4c.

though with negative values in the upper-left corner where TCs are intense but the pre-storm SST is low. This is not a typical situation since greater TC intensity generally corresponds to larger SST and causes stronger SSC (Supplementary Fig. 9), which merely accounts for a small portion of all data samples (Supplementary Fig. 9). This may occur as TCs cross over warm core eddies that act as an insulator between TC and subsurface cold water so that the relationship between TC intensity and underlying pre-storm SST can be altered<sup>34</sup>. For most cases, the TC rainfall is positively related to SST anomaly, reflecting that TC rain rate becomes smaller as the SSC is stronger. The differences of rain rates between the smallest (0–5%) and largest (95%–100%) magnitudes of SST anomaly data samples further consolidate such a phenomenon (Supplementary Fig. 10). Therefore, the TC-induced SST anomaly is indicated to be another contributor to TC rainfall other than TC intensity and environmental conditions.

To understand how the TC-induced SST anomaly contributes to changes in TC rainfall, the differences in surface enthalpy and boundary layer moisture between the smallest (0–5%) and largest (95%–100%) magnitudes of SST anomaly are further examined (Fig. 3). Given similar TC intensity and pre-storm SST, stronger SSC tends to induce smaller sea-to-air disequilibrium of moisture and temperature (Supplementary Fig. 11). The former diminishes surface evaporation and the latter cools the boundary layer airflow, both leading to a significant decrease of surface enthalpy transfer (Fig. 3). As a consequence, the boundary layer tends to be mostly less moist as the TC-induced SSC is stronger, which is not favorable for rain activities of TCs.

The TC-induced SST anomaly exhibits a typical rightward biased pattern, possessing a maximum near the storm center (Fig. 4a).

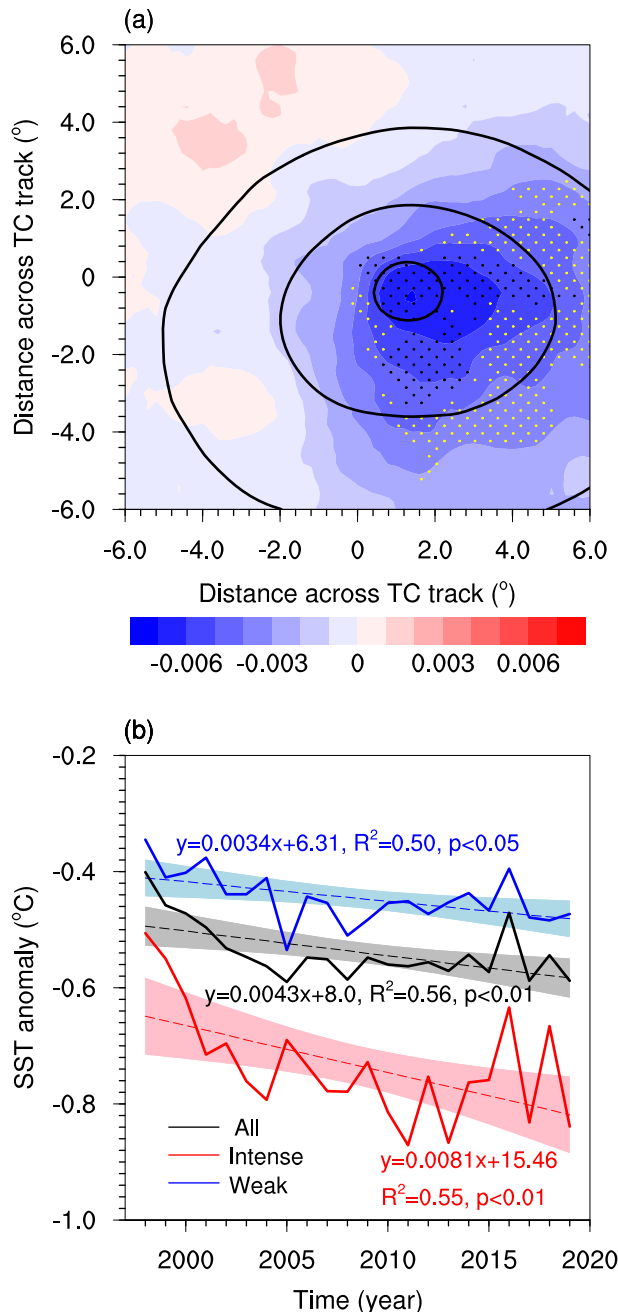


**Fig. 4 Increasing magnitude trend of TC-induced sea surface cooling.** **a** Spatial distribution of composite TC-induced SST anomaly ( $^{\circ}\text{C}$ ; contour) and change rate of TC-induced SST anomaly ( $^{\circ}\text{C year}^{-1}$ ; shaded). The SST anomaly is at an interval of  $-0.2^{\circ}\text{C}$ , with the outmost contour being  $-0.2^{\circ}\text{C}$ . Stippling denotes an area where linear trends are statistically significant, with black and yellow dots representing 99% and 95% confidence levels, respectively. **b** Time series of area-averaged SST anomaly ( $^{\circ}\text{C}$ ) within a radius of 200 km from TC center for all TCs, intense TCs (cat 1–5), and weak TCs (cat 0). The linear fitting function and correlation coefficient in (b) are also shown.

The increasing magnitude trend of negative SST anomalies over the cold wake is mostly statistically significant, being most remarkable at the right side of the storm center. An area averaging shows statistically significant strengthening of SSC caused by TCs (Fig. 4b). On average, the TC-induced SSC increases by  $0.0043^{\circ}\text{C}$  per year, amounting to  $\sim 0.8\%$  of the averaged magnitude of SST anomaly. The increasing trend becomes much

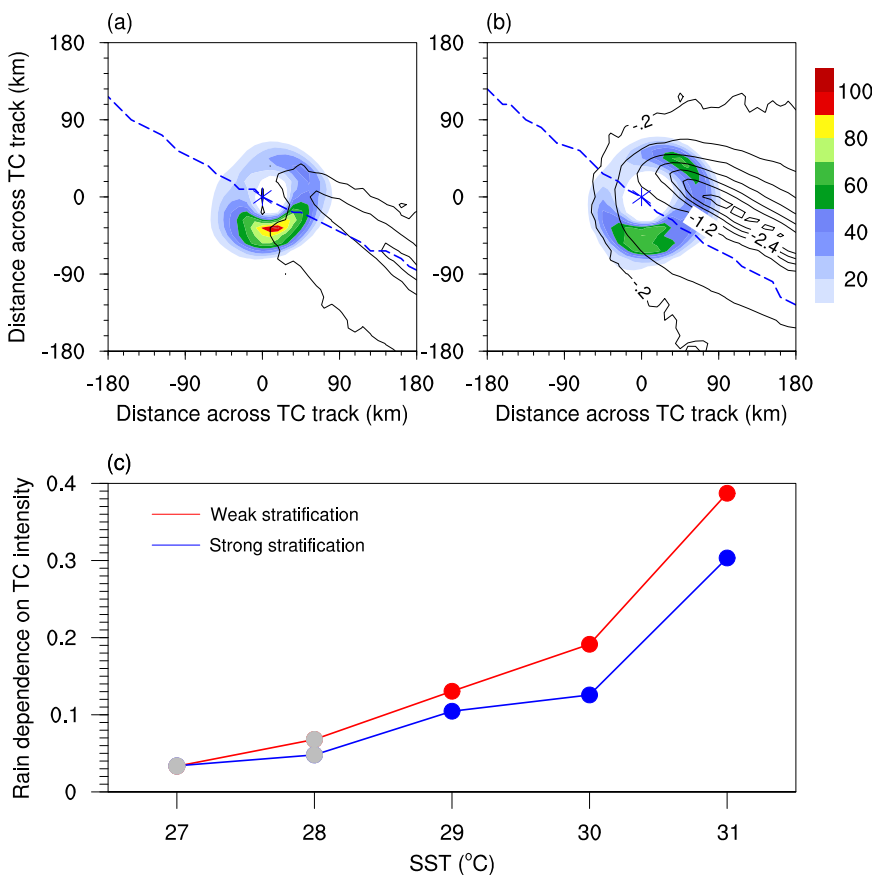


**Fig. 5 Discrepancy of TC rainfall with differing SST anomaly from model simulations.** Spatial distribution of rain rate ( $\text{mm h}^{-1}$ ; shaded) and SST anomaly ( $^{\circ}\text{C}$ ; black contour) for (a) weak stratification experiment and (b) strong stratification experiment with the pre-storm SST being  $29^{\circ}\text{C}$ . Simulation times shown for (a) and (b) are 45 h and 60 h, respectively, both of which correspond to the same maximum surface wind of  $50 \text{ m s}^{-1}$ . Blue dashed lines in (a) and (b) denote the simulated storm tracks, respectively. c Change rate of TC rainfall ( $\text{mm h}^{-1} \text{s m}^{-1}$ ) as a function of TC intensity (maximum surface wind) for weak and strong stratification experiments with the pre-storm SST setting to  $27\text{--}31^{\circ}\text{C}$  at an interval of  $1^{\circ}\text{C}$ . Blue and red dots denote the experiments in which the dependence of TC rainfall change rate on maximum surface wind is statistically significant above the 99% confidence level. Gray dots denote the experiments that fail to pass the significant test.

more pronounced for intense TCs than for weak TCs, increasing from  $0.0034^{\circ}\text{C}$  per year to  $0.0081^{\circ}\text{C}$  per year. This explains well the stronger decreasing trend of TC rainfall with more intense TCs (Fig. 1b).

To further investigate the possible influence of TC-induced SST anomaly on rain rate, a series of numerical simulations are conducted. An idealized TC translating northwest over a horizontally uniform sea surface is designed and conducted using the Weather Research and Forecasting (WRF) model by coupling a simple mixed layer ocean model (See methods). The experiments with weak and strong stratifications, and therefore weak and strong oceanic responses, are compared with varying pre-storm SST. As the SSC is stronger, the TC intensity is weaker, and the rain rate is also smaller (Supplementary Fig. 12). Of interest is that even with the same intensity, the TC rainfall is still notably smaller for stronger SSC (Fig. 5a, b), supporting the statistical result from satellite datasets that SST anomaly is a potentially important contributor to TC rainfall (Fig. 2). The positive dependence of rainfall on TC intensity increases steadily with increasing pre-storm SST, indicating that TC rain rate will increase faster with TC intensity at higher SST (Fig. 5c). Besides, the increasing rate of rainfall with TC intensity is overall larger for weaker SSC, with the discrepancy between weak and strong stratifications tending to be larger for higher pre-storm SST. As shown in Supplementary Fig. 13, weaker SSC has induced a much larger surface enthalpy flux, wherein surface latent heat flux moistens the TC system and surface sensible heat flux heats the low-level atmosphere.

Consequently, the boundary layer becomes moister, and the convection tends to be overall more intense. This is consistent with the statistical results reflected by Fig. 3, and explains the dependence of TC rainfall on TC's cold wake.

## DISCUSSION

From the energetic perspective, diabatic heating occurring in TCs is the dominant energy source fueling the development and maintenance of TCs, and can be promisingly estimated by surface precipitation. The inconsistent trends between decreasing inner-core rain rate and non-decreasing TC intensity (Fig. 1b and Supplementary Fig. 8) reveal that there must be a compensating process at work, namely the increasing diabatic heating in the outer region of TCs. The change rate of rainfall in the outer region is positive for the TRMM product but approaches near zero for the GPM product. Given the robust increasing trend of environmental rainfall with global warming, the TRMM product is indicated to be capable of better reflecting the evolutionary trend of rainfall than the GPM product, though it underestimates heavy precipitation<sup>35</sup>.

The increasing environmental SST not only heats the atmosphere but also causes more evaporation<sup>36</sup>. The favorable large-scale environment of rising SST and total precipitable water has led to an increase in rainfall for the whole TC system, as recently noted by Guzman and Jiang<sup>21</sup>. During the time period of 1998–2019, the TC rainfall increased at a rate of  $0.017 \text{ mm h}^{-1}$  per year on average, corresponding to a percentage  $\sim 7.6\%$  each

decade. However, the background rainfall increases at a rate of  $0.024 \text{ mm h}^{-1}$  per year, being 40% larger than the TC rainfall, an indication of a relative decreasing rainfall trend of TCs relative to the background environment. The discrepancy would be much larger if a smaller averaging radius were chosen (Fig. 2a).

Comparisons of radial distributions of rainfall change rate reveal that the deviation of TCs from the background environment enlarges radially inward monotonically, turning to be negative within  $1\text{--}2^\circ$  radius and reaching a maximum near the storm center. Kim et al.<sup>37</sup> and Guzman and Jiang<sup>21</sup> noted that the influence of large-scale environmental conditions on TC rainfall is more salient in the outer region than in the inner region, the latter of which relies primarily on TC intensity. Therefore, the overall increasing trend of TC rainfall is predominantly subject to a favorable large-scale environment, and there is a net decreasing trend of TC rainfall relative to the background rainfall.

TC rain rate increases steadily with pre-storm SST, even if the TC intensity is unchanged. After isolating the effect of TC intensity and pre-storm SST, the TC-induced SST anomaly is found to be another potential contributor to TC rainfall, with stronger SSC corresponding to smaller rainfall. This is because the SSC reduces the upward transport of surface enthalpy, and therefore the boundary layer moisture in TCs is decreased. The change rate of TC rainfall is found to rely closely on that of SST anomaly. As a result, the rain rate in the inner core of TCs has decreased in recent 22 years due to the strengthening TC's cold wakes. Note that there are compensating effects between the rising background SST that increases rain rate and the strengthening SSC that diminishes rain rate. It remains unclear to what extent the positive role of rising background SST will be compensated by the negative role of strengthening SSC in a warming future, which may be worth further investigation. Future work may also extend to a longer time period of observations to diagnose the separate contributions of natural variability and anthropogenic activities, e.g., using the land-based rain-gauge data<sup>38</sup>, with a focus on the landfalling TCs.

In conclusion, this study highlights that although TC rainfall has been increasing over the past two decades, there is a net decreasing rainfall trend of TCs relative to the background environment. The TC-induced SSC is suggested to be an important contributor to TC rainfall, which has been neglected in most climate modeling studies. To improve TC rainfall projections, the TC-ocean interaction should be well resolved in global and regional climate models.

## METHODS

### Data

Global rainfall data are obtained from 3-h TRMM 3B42 product<sup>39</sup> at spatial resolutions of  $0.25^\circ \times 0.25^\circ$ , available from January 1998 to December 2019, and from 3-h GPM IMERG product<sup>40</sup> at spatial resolutions of  $0.1^\circ \times 0.1^\circ$ , available from June 2000 to September 2021. TC information including storm location and the maximum surface wind is derived from the 3-h best track data of the International Best Track Archive for Climate Stewardship (IBTrACS) dataset<sup>41</sup>. To keep data consistency, the data from US agencies are used to cover global TCs. All TCs with maximum surface wind greater than  $15 \text{ m s}^{-1}$  are considered. In combination with the best track data, the time periods of 1998–2019 and 2001–2020 are selected for TRMM and GPM datasets, corresponding to 117061 and 102258 observations, respectively. Considering the through-cloud capability of microwave measurements, SST is obtained from the Optimal Interpolation microwave product of remote sensing systems, which has a temporal resolution of 1 day and spatial resolutions of  $0.25^\circ \times 0.25^\circ$ , available since 1998. The same time periods of 1998–2019 and 2001–2020 as TRMM and GPM products are used for SST data, respectively. Surface air

temperature and water vapor mixing ratio data are obtained from the Atmospheric Infrared Sounder (AIRS) version 6 product at temporal resolution of 1 day and spatial resolutions of  $1^\circ \times 1^\circ$ , available since August 2002. The boundary layer column water vapor comes from the Advanced Microwave Scanning Radiometer and Moderate Resolution Imaging Spectroradiometer (AMSR-MODIS) product at temporal resolution of 1 day and spatial resolutions of  $1^\circ \times 1^\circ$ , available from July 2002 to 2017. For the calculations of air-sea temperature moisture difference, and boundary layer moisture, the time periods of 2002–2019 and 2002–2017 are used.

### Calculations of TC rainfall, background rainfall, and SST anomaly

For each 3-h TC location, a square domain is defined with widths of  $20^\circ$  at spatial resolutions of  $0.2^\circ \times 0.2^\circ$ , centered on the TC location<sup>33</sup>. The bottom and top boundaries are perpendicular to the zonal direction, while the left and right boundaries are parallel to the zonal direction. Given that large-scale SST decreases poleward in both hemispheres, the domain in the Southern Hemisphere is overturned so that the top boundaries in all domains point to the poleward direction; the left boundary points to the westward and eastward direction in the Northern and Southern Hemispheres, respectively. All precipitation and SST data are bilinearly interpolated into the domains and are then classified according to TC intensity, SST anomaly, etc. For each grid in the domain, an averaging is taken for all rainy events within a specified year; linear fitting and statistical tests are performed over the whole time period grid by grid. For radial distribution of rainfall change rate, the variable obtained from linear fitting is firstly transformed into polar coordinates over the domain, and then azimuthal averaging is taken with the storm center as the coordinate origin. For area averaging, all rainy grids are searched and summed up within a certain radius threshold (e.g., 500 km) from the storm center, and are divided by the number of grids meet the requirement.

The background rainfall is obtained with the same domain definition as the TC rainfall, but with the precipitation data shifted from one year before. By doing so, the time period of background rainfall is 1999–2019 and 2002–2020 for TRMM and GPM products, respectively, covering time periods one year shorter than those of TC rainfall. The background rainfall changes thereby denote the changes in climatological rainfall in the regions where TCs occur, with rainfall from all sources being included. We also tested an average of the previous 3 years to construct the background rainfall, wherein two and one years are used for 2020 and 1999, respectively. The calculated change rate of background rainfall is nearly the same as that from 1-year calculation (Supplementary Fig. 14). The relative rainfall is obtained by subtracting the background rainfall from the TC rainfall (Fig. 1d). The SST anomaly (Figs. 2 and 4) is calculated by the SST at the day of TC passage minus the pre-storm value, which is defined as an average between  $-5$  and  $-3$  days relative to TC passage.

The TC positions from the best track dataset bear uncertainties at  $\sim 10\text{--}40 \text{ km}$ <sup>42</sup>, which may interfere with the spatial distributions of TC rainfall. Nonetheless, the bias from random errors of best track positions could be largely alleviated by the large data sampling. To exclude the interference from possible systematical bias of the data sources, results from two TC position products are compared, with one from the US agency product and the other one from the IBTrACS merged product (Supplementary Fig. 15). Both show nearly the same distributions of TC rainfall and rain rate, indicating that the influence from TC position uncertainties could be not distinct. TCs both over the ocean and land are incorporated in Fig. 1, while the relationship between TC rainfall and SST anomaly exists over the ocean. The cases over the ocean account for  $\sim 94\%$  of all data samples. A comparison between the

results from all TCs and TCs over the ocean (Supplementary Fig. 16) suggests that the decreasing trend of TC rainfall becomes slightly stronger in the inner core of TCs after removing landfalling TCs.

## Calculations of surface enthalpy deficit

The enthalpy of  $k$  is defined as:

$$k = c_p T + L_v q, \quad (1)$$

where  $c_p$  is the specific heat at constant pressure,  $L_v$  is the latent heat of vaporization,  $T$  is temperature, and  $q$  is the water vapor mixing ratio. The sea-to-air surface enthalpy deficit can thus be obtained by:

$$\Delta k = c_p (SST - T_a) + L_v (q_s - q_a). \quad (2)$$

The subscripts  $s$  and  $a$  denote sea surface and surface air, respectively.  $q_s$  is calculated via a conventional formula that is positively related to SST and negatively related to surface pressure, taken as 1000 hPa for simplicity. The surface temperature and moisture disequilibrium as well as enthalpy deficit can be calculated using SST, surface temperature, and water vapor mixing ratio datasets. In a bulk formula framework, surface sensible flux (SHX) and surface latent heat flux (LHX) are determined by  $SHX = \rho c_p C_k U_{10} (SST - T_a)$  and  $LHX = \rho L_v C_k U_{10} (q_s - q_a)$ , where  $\rho$  is density,  $C_k$  is surface enthalpy coefficient, and  $U_{10}$  is surface wind. Therefore, the surface enthalpy deficit, including surface temperature and moisture disequilibrium, is crucial to TC development since it determines how much heat and moisture can be transported upward at a given TC intensity.

## Statistical test

The simple linear regression is used to estimate the change rate as well as linear fitting. The statistical trend with time is examined using the Mann–Kendall test. The relation between two independent variables is tested by calculating the correlation coefficient.

## Numerical experiments

The rainfall of TCs in response to SST anomaly is simulated using the WRF model version 3.7.1<sup>43</sup> by coupling with a simple mixed layer ocean model<sup>44</sup>. Physical schemes chosen for configuring the model are listed in Supplementary Table 1. The model domain possesses dimensions of  $400 \times 370$  with horizontal resolutions of 9 km. A total of 45 levels are placed as default in the vertical direction. The model is set on a  $\beta$  plane with the model domain center set at 20°N. For the initialization of idealized TCs, a horizontally uniform ambient environment is specified with the temperature, humidity, and geopotential height fields coming from the mean tropical sounding of Jordan<sup>45</sup>. The underlying surface is uniformly ocean surface, with a sea level pressure of 1010 hPa. The uniform easterly winds of  $3 \text{ m s}^{-1}$  are specified at all levels, with geopotential heights adjusted according to the geostrophic wind balance. A Rankine vortex with a maximum surface wind of  $19 \text{ m s}^{-1}$  at 100-km radius is then inserted into the idealized environment. The initial vortex is at hydrostatic and gradient wind balances. The model is integrated for a total of 120 h with the output at an interval of 1 h. The simulated TCs move northwest under the easterly steering flow and the beta effects (Fig. 5).

A total of five groups of sensitivity experiments are conducted, with the pre-storm SST setting to 27 °C, 28 °C, 29 °C, 30 °C, and 31 °C. For each group, two experiments with weak and strong stratifications are set, with their details listed in Supplementary Table 2. Previous observations show that TC-induced SSC varies in a large span from less than 1 °C to as large as 9 °C<sup>46,47</sup>. The simulated SSC is well within the observational range (Fig. 5). Since the maximum 10-m surface wind output by the model is a

transient value but a short-time average by the best track data, we use the azimuthal mean wind to denote TC intensity to avoid random noises.

## DATA AVAILABILITY

The TRMM 3B42 precipitation product is obtained from [https://disc2.gesdisc.eosdis.nasa.gov/opendap/hyrax/TRMM\\_L3/TRMM\\_3B42.7/](https://disc2.gesdisc.eosdis.nasa.gov/opendap/hyrax/TRMM_L3/TRMM_3B42.7/). The GPM IMERG product is obtained from [https://gpm1.gesdisc.eosdis.nasa.gov/opendap/hyrax/GPM\\_L3/GPM\\_3IMERGDF.06/](https://gpm1.gesdisc.eosdis.nasa.gov/opendap/hyrax/GPM_L3/GPM_3IMERGDF.06/). The IBTrACS best track dataset is obtained from <https://www.ncei.noaa.gov/products/international-best-track-archive>. The SST product is obtained from <https://data.remss.com/SST/daily/mw/v05.1/>. The AIRS v6 product is obtained from [https://acdsc.gesdisc.eosdis.nasa.gov/opendap/hyrax/Aqua\\_AIRS\\_Level3/AIRS3STD.006/](https://acdsc.gesdisc.eosdis.nasa.gov/opendap/hyrax/Aqua_AIRS_Level3/AIRS3STD.006/). The AMSR-MODIS product is obtained from <https://measures.gesdisc.eosdis.nasa.gov/data/BLWV/AMDBLWV.2/>. All processed data used during the study are available on request from the authors.

## CODE AVAILABILITY

All codes for data processing and figure presentation are available from the corresponding author on reasonable request.

Received: 10 March 2023; Accepted: 17 August 2023;

Published online: 05 September 2023

## REFERENCES

1. Jiang, H. & Zipser, E. J. Contribution of tropical cyclones to the global precipitation from eight seasons of TRMM data: regional, seasonal, and interannual variations. *J. Clim.* **23**, 1526–1543 (2010).
2. Khouakhi, A., Villarini, G. & Vecchi, G. A. Contribution of tropical cyclones to rainfall at the global scale. *J. Clim.* **30**, 359–372 (2017).
3. Rappaport, E. N. Loss of life in the United States associated with recent Atlantic tropical cyclones. *Bull. Am. Meteor. Soc.* **81**, 2065–2074 (2000).
4. Rappaport, E. N. Fatalities in the United States from Atlantic Tropical Cyclones: new data and interpretation. *Bull. Am. Meteor. Soc.* **95**, 341–346 (2014).
5. Pielke, R. A. et al. Normalized hurricane damage in the United States: 1900–2005. *Nat. Hazards Rev.* **9**, 29–42 (2008).
6. Lonfat, M., Marks, F. D. J. & Chen, S. S. Precipitation distribution in tropical cyclones using the tropical rainfall measuring mission (TRMM) microwave imager: a global perspective. *Mon. Wea. Rev.* **132**, 1645–1660 (2004).
7. Lonfat, M., Rogers, R., Marchok, T. & Marks, F. D. A parametric model for predicting hurricane rainfall. *Mon. Wea. Rev.* **135**, 3086–3097 (2007).
8. Kim, D., Ho, C., Park, D., Chan, J. & Jung, Y. The relationship between tropical cyclone rainfall area and environmental conditions over the subtropical oceans. *J. Clim.* **31**, 4605–4616 (2018).
9. Tu, S. et al. Increase in tropical cyclone rain rate with translation speed. *Nat. Commun.* **13**, 7325 (2022).
10. Jiang, H., Halverson, J. B. & Zipser, E. J. Influence of environmental moisture on TRMM-derived tropical cyclone precipitation over land and ocean. *Geophys. Res. Lett.* **35**, L17806 (2008).
11. Hill, K. A. & Lackmann, G. M. Influence of environmental humidity on tropical cyclone size. *Mon. Wea. Rev.* **137**, 3294–3315 (2009).
12. Matyas, C. J. Associations between the size of hurricane rain fields at landfall and their surrounding environments. *Meteor. Atmos. Phys.* **106**, 135–148 (2010).
13. Lin, Y., Zhao, M. & Zhang, M. Tropical cyclone rainfall area controlled by relative sea surface temperature. *Nat. Commun.* **6**, 6591 (2015).
14. Allen, M. R. & Ingram, W. J. Constraints on future changes in climate and the hydrologic cycle. *Nature* **419**, 224–232 (2002).
15. Zhang, W. et al. Increasing precipitation variability on daily-to-multiyear time scales in a warmer world. *Sci. Adv.* **7**, eabf8021 (2021).
16. Knutson, T. R. et al. Simulated reduction in Atlantic hurricane frequency under twenty-first-century warming conditions. *Nat. Geosci.* **1**, 359–364 (2008).
17. Knutson, T. R. et al. Tropical cyclones and climate change. *Nat. Geosci.* **3**, 157–163 (2010).
18. Knutson, T. R. et al. Tropical cyclones and climate change assessment. Part II: projected response to anthropogenic warming. *Bull. Am. Meteor. Soc.* **101**, E303–E322 (2020).
19. Villarini, G. et al. Sensitivity of tropical cyclone rainfall to idealized global scale forcings. *J. Clim.* **27**, 4622–4641 (2014).
20. Liu, M., Vecchi, G., Smith, J. & Knutson, T. Causes of large projected increases in hurricane precipitation rates with global warming. *NPJ Clim. Atmos. Sci.* **2**, 38 (2019).

21. Guzman, O. & Jiang, H. Global increase in tropical cyclone rain rate. *Nat. Commun.* **12**, 5344 (2021).
22. Tu, S. et al. Recent global decrease in the inner-core rain rate of tropical cyclones. *Nat. Commun.* **12**, 1948 (2021).
23. Shapiro, L. J. & Willoughby, H. E. The response of balanced hurricanes to local sources of heat and momentum. *J. Atmos. Sci.* **39**, 378–394 (1982).
24. Ma, Z. A study of the interaction between Typhoon Francisco (2013) and a cold core eddy. Part I: rapid weakening. *J. Atmos. Sci.* **77**, 355–377 (2020).
25. Huang, P., Lin, I.-I. & Huang, R. Change in ocean subsurface environment to suppress tropical cyclone intensification under global warming. *Nat. Commun.* **6**, 7188 (2015).
26. Da, N., Foltz, G. & Balaguru, K. Observed global increases in tropical cyclone-induced ocean cooling and primary production. *Geophys. Res. Lett.* **48**, e2021GL092574 (2021).
27. Emanuel, K. A. Effect of upper-ocean evolution on projected trends in tropical cyclone activity. *J. Clim.* **28**, 8165–8170 (2015).
28. Tuleya, R. E. et al. Impact of upper tropospheric temperature anomalies and vertical wind shear on tropical cyclone evolution using an idealized version of the operational GFDL hurricane model. *J. Atmos. Sci.* **73**, 3803–3820 (2016).
29. Larson, J., Zhou, Y. & Higgins, R. W. Characteristics of landfalling tropical cyclones in the United States and Mexico: climatology and interannual variability. *J. Clim.* **18**, 1247–1262 (2005).
30. Jiang, H., Liu, C. & Zipser, E. J. A TRMM-based tropical cyclone cloud and precipitation feature database. *J. Appl. Meteor. Climatol.* **50**, 1255–1274 (2011).
31. Wei, N., Song, J., Dai, Y., Jiang, S. & Duan, Y. Recent decrease in inner-core rain rate of tropical cyclones over the western North Pacific. *Atmos. Sci. Lett.* **23**, e1125 (2022).
32. Xu, J. & Wang, Y. Sensitivity of tropical cyclone inner-core size and intensity to the radial distribution of surface entropy flux. *J. Atmos. Sci.* **67**, 1831–1852 (2010).
33. Ma, Z., Fei, J., Lin, Y. & Huang, X. Modulation of clouds and rainfall by tropical cyclone's cold wakes. *Geophys. Res. Lett.* **47**, e2020GL088873 (2020).
34. Lin, I.-I. et al. The interaction of Super typhoon Maemi with a warm ocean eddy. *Mon. Wea. Rev.* **133**, 2635–2649 (2005).
35. Chen, Y., Ebert, E. E., Walsh, K. J. E. & Davidson, N. E. Evaluation of TMPA 3b42 daily precipitation estimates of tropical cyclone rainfall over Australia. *J. Geophys. Res.: Atmos.* **118**, 11966–11978 (2013).
36. Trenberth, K., Dai, A., Rasmusson, R. & Parsons, D. The changing character of precipitation. *Bull. Am. Meteor. Soc.* **84**, 1205–1217 (2003).
37. Kim, D., Ho, C.-H., Murakami, H. & Park, D.-S. R. Assessing the influence of large-scale environmental conditions on the rainfall structure of Atlantic tropical cyclones: an observational study. *J. Clim.* **34**, 2093–2106 (2021).
38. Westra, S., Alexander, L. V. & Zwiers, F. W. Global increasing trends in annual maximum daily precipitation. *J. Clim.* **26**, 3904–3918 (2013).
39. Huffman, G. J., Adler, R. F., Bolvin, D. T. & Nelkin, E. J. The TRMM multisatellite precipitation analysis (TMPA): Quasi-global, multiyear, combined-sensor precipitation estimates at fine scales. *J. Hydrometeor* **8**, 38–55 (2007).
40. Huffman, G. J. et al. Integrated multi-satellite retrievals for the global precipitation measurement (GPM) mission (IMERG), satellite precipitation measurement. *Springer. Int. Publ.* **1**, 343–353 (2020).
41. Knapp, K. R., Kruk, M. C., Levinson, D. H., Diamond, H. J. & Neumann, C. J. The international best track archive for climate stewardship (IBTrACS): unifying tropical cyclone best track data. *Bull. Am. Meteor. Soc.* **91**, 363–376 (2010).
42. Kruk, M. C., Knapp, K. R. & Levinson, D. H. A technique for combining global tropical cyclone best track data. *J. Atmos. Ocean. Tech.* **27**, 680–692 (2010).
43. Skamarock, W. C. et al. A description of the advanced research WRF version 3. NCAR Tech. Note NCAR/TN-475+STR, 113pp (2008).
44. Pollard, R. T., Rhines, P. B. & Thompson, R. O. R. Y. The deepening of the wind-mixed layer. *Geophys. Astrophys. Fluid Dyn.* **4**, 381–404 (1973).
45. Jordan, C. L. Mean soundings for the West Indies area. *J. Meteor.* **15**, 91–97 (1958).
46. Lin, I.-I. et al. New evidence for enhanced primary production triggered by tropical cyclone. *Geophys. Res. Lett.* **30**, 1718 (2003).
47. Mei, W. & Pasquero, C. Spatial and temporal characterization of sea surface temperature response to tropical cyclones. *J. Clim.* **26**, 3745–3765 (2013).

## ACKNOWLEDGEMENTS

This work is supported by the National Natural Science Foundation of China with Grant 42022033, 42130603, and 42192552.

## AUTHOR CONTRIBUTIONS

Z.M. and Y.L. conceived the idea. Z.M. performed the analysis and wrote the paper. Y.L. wrote the paper and supervised the findings of this work. All authors discussed the results and edited the manuscript.

## COMPETING INTERESTS

The authors declare no competing interests.

## ADDITIONAL INFORMATION

**Supplementary information** The online version contains supplementary material available at <https://doi.org/10.1038/s41612-023-00460-w>.

**Correspondence** and requests for materials should be addressed to Yanluan Lin.

**Reprints and permission information** is available at <http://www.nature.com/reprints>

**Publisher's note** Springer Nature remains neutral with regard to jurisdictional claims in published maps and institutional affiliations.



**Open Access** This article is licensed under a Creative Commons Attribution 4.0 International License, which permits use, sharing, adaptation, distribution and reproduction in any medium or format, as long as you give appropriate credit to the original author(s) and the source, provide a link to the Creative Commons license, and indicate if changes were made. The images or other third party material in this article are included in the article's Creative Commons license, unless indicated otherwise in a credit line to the material. If material is not included in the article's Creative Commons license and your intended use is not permitted by statutory regulation or exceeds the permitted use, you will need to obtain permission directly from the copyright holder. To view a copy of this license, visit <http://creativecommons.org/licenses/by/4.0/>.

© The Author(s) 2023